SUPPORTING INFORMATION

One-Pot Solvothermal Conversion of Polysilazane to Fluorescent Nanoparticles for Anticounterfeiting and Ag^+ Sensing Application

Amrita Chatterjee[a], Sushmit Sen[a], Keshav Dev[b], Pradip K. Maji[a*]

[a]Department of Polymer and Process Engineering, Indian Institute of Technology Roorkee, Saharanpur Campus, Saharanpur- 247001, India

[b]Department of Chemistry, Indian Institute of Technology Roorkee, Roorkee-247667, India

***Corresponding Author**: Pradip K. Maji (Email ID: pradip@pe.iitr.ac.in)

Contact no: +91-7895965010

Section S1: Materials

Toluene was purchased from TCI India. Polysilazane grade Durazane 1500 slow cure (Merck, Germany) was kindly supplied by SBL Specialty Coatings Private Limited. The chemicals were used without further purification.

Section S2: Characterization methods

Fourier-transform infrared (FTIR) spectroscopy was used to analyze the chemical structure and bonding evolution of the polysilazane-derived nanoparticles. FTIR spectra were recorded using a PerkinElmer Spectrum Two spectrometer in universal attenuated total reflectance (UATR) mode over a wavenumber range of 400–4000 cm^{-1} with a resolution of 4 cm^{-1}.

X-ray diffraction (XRD) measurements were performed using a Rigaku Ultima IV diffractometer (Japan) equipped with a Cu $K\alpha_1$ radiation source (λ = 1.5406 Å) operated at 40 kV. Diffraction patterns were collected over a 2θ range of 5°–55° at a scanning rate of 4° min^{-1} to evaluate the structural nature and crystallinity of the samples.

X-ray photoelectron spectroscopy (XPS) was conducted using a PHI-5000 VersaProbe III spectrometer (ULVAC-PHI Inc.) with Al Kα radiation as the excitation source. Survey spectra were acquired at a pass energy of 280 eV, while high-resolution spectra were recorded at a pass energy of 55 eV. The binding energies were calibrated using the C 1s peak at 284.6 eV as the reference, and the chemical states of Si, C, N, and O were analyzed accordingly.

SUPPORTING INFORMATION

The surface morphology of the nanoparticles was examined by field-emission scanning electron microscopy (FE-SEM, TESCAN MIRA3) operated at an accelerating voltage of 5–10 kV. Prior to imaging, the samples were sputter-coated with a thin layer of gold using a Quorum SC7620 sputter coater under high-vacuum conditions.

Transmission electron microscopy (TEM) was employed to investigate the particle morphology and size distribution using an FEI Tecnai G2 20 S-Twin microscope. For TEM analysis, a dilute nanoparticle suspension (0.0001 wt %) was drop-cast onto a 200-mesh copper grid and allowed to dry under ambient conditions.

Ultraviolet-visible absorption spectra were recorded using a Shimadzu UV-2600 spectrophotometer. Photoluminescence measurements were carried out on a Cary Eclipse fluorescence spectrophotometer (Agilent Technologies) equipped with a xenon lamp as the excitation source.

Section S3: Transformation of polysilazane to nanostructure

Under solvothermal conditions at 200 °C, polysilazane undergoes a series of coupled reactions leading to the formation of Si-rich amorphous nanoparticles. The transformation is initiated by hydrolysis of the Si–N backbone (Si–N + H_2O → Si–OH + NH_3), accompanied by transamination reactions that facilitate the rearrangement and gradual removal of nitrogen-containing species. Concurrently, reactive Si–H groups undergo dehydrogenation and oxidation, generating additional silanol (Si–OH) functionalities. These silanol groups subsequently participate in condensation (polymerization/crosslinking) reactions (Si–OH + Si–OH → Si–O–Si + H_2O), resulting in the formation of a progressively interconnected siloxane network.[1] In parallel, the organic substituents attached to silicon undergo partial decomposition and rearrangement, contributing to the formation of Si–O–C linkages and disordered carbon domains within the structure. During this polymer-to-ceramic conversion, nitrogen is largely eliminated as volatile species (e.g., NH_3), leading to an oxygen-dominated chemical environment.[2] The overall process yields an amorphous Si–O–C–N hybrid network, structurally characterized by a dominant Si–O_x framework with residual carbon and trace nitrogen, consistent with the spectroscopic observations.[3]

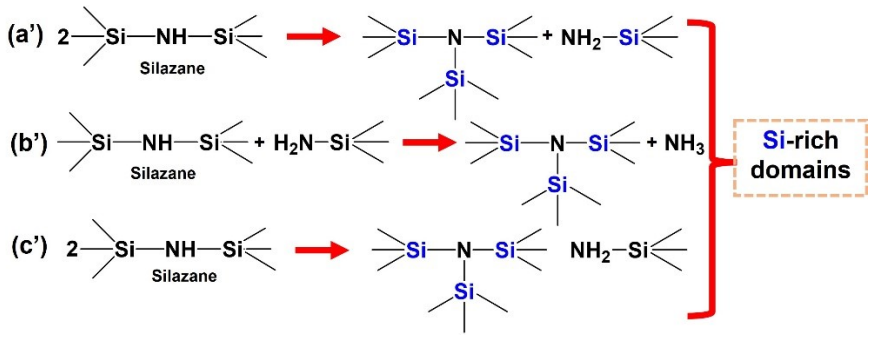

Figure 1S: Reaction pathways of polysilazanes

Section S4: Discussion on Defect-Mediated Photoluminescence

The photoluminescence observed in the present SiO_x-rich nanoparticles is attributed to defect- and surface-state-mediated transitions, which are widely reported in amorphous silica and related silicon-based systems. Previous studies have established that various intrinsic and extrinsic defect centers within disordered Si–O networks can act as emissive states. For example, Saita et al. demonstrated that fluorescence in silica-based nanoparticles originates from surface defect pairs such as dioxasilyrane (=Si(O_2)) and silylene (Si) centers, with hydrothermal treatment promoting defect formation and enhancing emission efficiency.[4]

Similarly, Guleria et al. reported that photoluminescence in amorphous SiO_2 nanoparticles arises from multiple defect states, particularly oxygen-related defects, which act as emission centers and can be tuned to produce emission across the blue-to-green spectral range.[5,6] The dominance of oxygen-deficient or oxygen-related defect states has also been correlated with enhanced emission intensity and sensing functionality in such systems. In polymer-derived systems, Menapace et al. showed that thermal treatment of polysilazane leads to visible photoluminescence, which is associated with structural rearrangements, dangling bonds, and the formation of carbon-related species during the polymer-to-ceramic transition.[7] These findings highlight the role of structural disorder and hybrid bonding environments (e.g., Si–O–C) in generating defect states capable of radiative recombination.

More advanced defect-engineered silica systems reported by Chang et al. and Sun et al. further demonstrate that both intrinsic defects (e.g., oxygen vacancies, non-bridging oxygen centers) and extrinsic impurities (e.g., carbon- or nitrogen-related species) contribute to a distribution of emissive states, resulting in complex optical behaviors including fluorescence and long-lived

phosphorescence.[8,9] Such studies emphasize that defect heterogeneity within amorphous silica networks is a key factor governing their photophysical properties. Additionally, Trillot et al. highlighted the presence of under-coordinated oxygen atoms in amorphous silica, which not only influence transport properties but also act as active sites for metal ion coordination.[10] These defect sites can interact strongly with ions such as Ag^{+} through O–Ag bonding, supporting their dual role in both optical emission and sensing behavior. Based on these established studies, the emission in the present system is attributed to a combination of oxygen-related defect centers, Si–O–C structural disorder, and residual defects generated during the solvothermal polymer-to-ceramic transformation. The observed excitation-dependent emission further supports the presence of a distribution of defect states rather than a single well-defined emissive center.

Section S5: Fluorescence Quantum Yield

As a reference, rhodamine 6G, which has a known quantum yield of .95, was used to calculate the quantum yield (QY) of polysilazane-derived nanoparticles. Both nanoparticles and rhodamine 6G solutions were made to keep their UV-Vis absorption peaks at or below 0.1. The fluorescence intensities were calculated by integrating the regions under the PL emission spectra, and the absorption and fluorescence spectra were taken at an excitation wavelength of 480 nm. The following (**Equation 1S**) was used to get the quantum yield of nanoparticles. The absorbance of both solutions was maintained below 0.1 to minimize inner filter effects. The quantum yield of the polysilazane-derived nanoparticles was calculated to be approximately 26%.

The following (**Equation 1S**) was used to get the quantum yield of the particle.

$$QY = QYs \times \frac{I}{Is} \times \frac{As}{A} \times \frac{\eta 2}{\eta s 2} \times 100\% \quad \text{) ..... (equation 1S)}$$

QY is the quantum yield of the particle. The quantum yield of rhodamine 6G, the reference, is denoted as *QYs*. The integral regions of the fluorescence peaks for the reference and the nanoparticles are denoted by *I* and *Is*, respectively. The absorbance values for the nanoparticles and the reference are *A* and *As*, respectively. These η represent the solvents' refractive indices.

Section S6: Dynamic light scattering (DLS) measurements

Dynamic light scattering measurements were carried out to evaluate the hydrodynamic size of the nanoparticles. The average particle size obtained from DLS is 100-105 nm, which is slightly higher

than the size observed from TEM (85-90 nm). This difference can be attributed to the hydrodynamic nature of DLS measurements, which include contributions from the solvation layer and surface-associated species, whereas TEM reflects the physical size of dried nanoparticles. The polydispersity index (PDI) of 0.3 indicates a moderately broad size distribution, and the intensity-weighted nature of DLS may also contribute to a slightly higher apparent size. Overall, the results confirm the formation of well-dispersed nanoparticles.

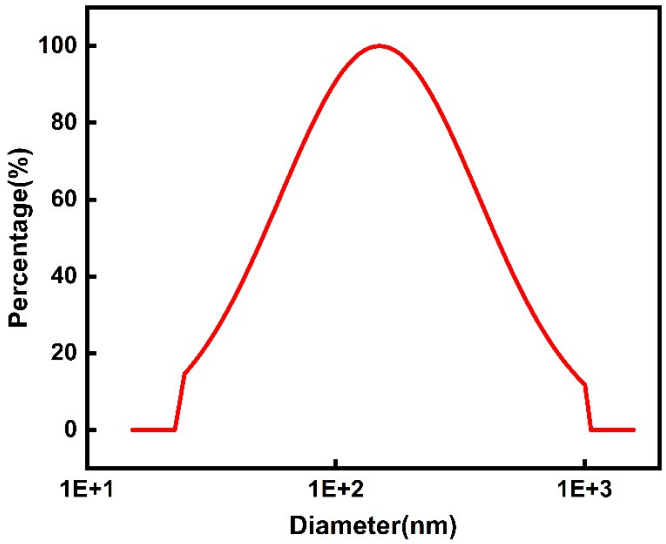

Figure 2S: DLS Study of the synthesized nanoparticles

Section S7: Comparison with other systems for the detection of Ag+

A comparison of the detection limit and linear sensing range of the present system with previously reported nanoparticle-based Ag^+ sensors. For instance, Luo et al. reported red-emissive carbon dots with a detection limit of 0.37 µM and a linear range of 0–50 µM, while Lu et al. developed dual-functional carbon dots exhibiting a lower detection limit of 0.05 µM.[11,12] Similarly, Zhang et al. demonstrated ratiometric carbon quantum dots with a detection limit of 0.14 µM and a wide linear range of 22–220 µM. In comparison, Wang et al. reported N-doped carbon dots with a relatively higher detection limit of 4.7 µM and a linear range of 30–210 µM.[13,14] Additionally, Wu et al. developed bisbenzimidazole-based fluorescent sensors exhibiting rapid and selective Ag^+ detection based on complexation-induced quenching.[15]

These comparisons indicate that the polysilazane-derived nanoparticles in the present study exhibit a competitive detection limit (0.55 μM) and a comparable sensing range relative to existing fluorescent nanomaterial-based systems. Notably, unlike conventional carbon-dot or small-molecule-based probes, the present system is derived from a single-source preceramic polymer via a one-pot solvothermal route, resulting in an oxygen-rich Si–O–C–N hybrid network. The sensing mechanism is governed by defect-rich siloxane environments rather than surface functional groups or molecular fluorophores, offering enhanced structural robustness, long-term stability, and potential compatibility with coating-based applications.

Section S8: Fluorescence lifetime study

The fluorescence decay profiles were fitted using a multi-exponential model, yielding three lifetime components for the pristine nanoparticles ($\tau_1 \approx 0.25$ ns, $\tau_2 \approx 1.11$ ns, and $\tau_3 \approx 2.93$ ns), with the longest-lived component accounting for ~67% of the total decay. Upon addition of Ag^+ ions, all lifetime components increased ($\tau_1 \approx 0.37$ ns, $\tau_2 \approx 1.95$ ns, and $\tau_3 \approx 4.74$ ns), along with a marked shift in relative amplitudes toward the longer-lived components ($\tau_2 \approx 48\%$ and $\tau_3 \approx 47\%$). Consequently, an overall increase in average fluorescence lifetime was observed despite the simultaneous decrease in emission intensity. This unusual behavior suggests that Ag^+ ions interact with surface-associated defect states, altering the emissive-state population and suppressing faster non-radiative decay channels. Together with Raman and XPS results confirming a defect-rich Si–O–C network containing abundant oxygen-bearing surface functionalities, these findings support a sensing mechanism dominated by defect-state modulation rather than simple dynamic collisional quenching. The fluorescence decay profiles were fitted using a multi-exponential model:

$$I(t) = B_1 e^{-t/\tau_1} + B_2 e^{-t/\tau_2} + B_3 e^{-t/\tau_3} \quad \text{…….. (equation 2S)}$$

where τ_i represent the lifetime components and B_i their relative contributions.

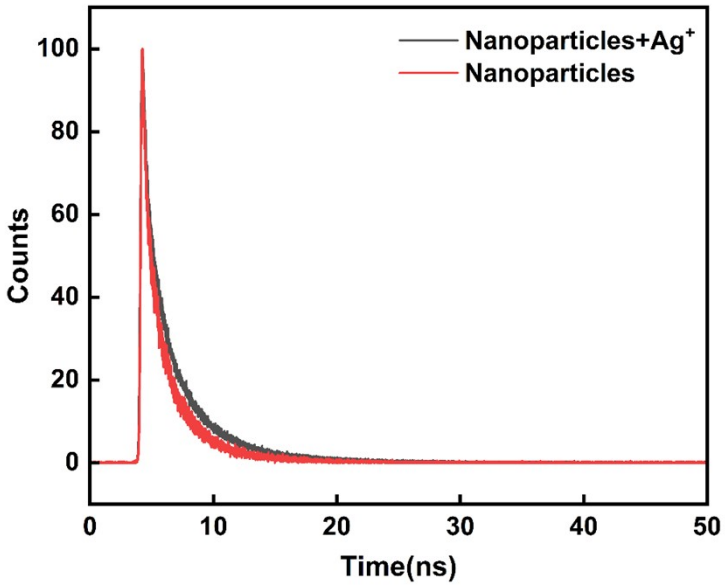

Figure 3S: Fluorescence lifetime study showing the slower decay of the excited states of the nanoparticles in combination of the Ag^{+} ions.

References:

(1) D'Elia, R.; Dusserre, G.; Del Confetto, S.; Eberling-Fux, N.; Descamps, C.; Cutard, T. Effect of Dicumyl Peroxide Concentration on the Polymerization Kinetics of a Polysilazane System. *Polym. Eng. Sci.* 2018, *58* (6), 859–869. https://doi.org/10.1002/PEN.24638;PAGE:STRING:ARTICLE/CHAPTER.

(2) Hwang, Y.; Ahn, K.; Kim, J. Silicon Carbonitride Covered SiC Composites for Enhanced Thermal Conductivity and Electrical Insulation. *Appl. Therm. Eng.* 2014, *70* (1), 600–608. https://doi.org/10.1016/J.APPLTHERMALENG.2014.05.015.

(3) Chatterjee, A.; Sen, S.; Ramakanth, D.; Singh, S.; Maji, P. K. Unravelling Polysilazanes: Synthesis, Structure-Property Insights and Versatile Coating Applications. *Adv. Colloid Interface Sci.* 2025, *342*, 103508. https://doi.org/10.1016/J.CIS.2025.103508.

(4) Saita, S.; Kawasaki, H. Origin of the Fluorescence in Silica-Based Nanoparticles Synthesized from Aminosilane Coupling Agents. *J. Lumin.* 2021, *232*, 117849. https://doi.org/10.1016/J.JLUMIN.2020.117849.

(5) Guleria, A.; Chavan, A. P.; Tomy, A.; Baby, C. M.; Neogy, S.; Debnath, A. K.; Adhikari, S. Defect Originated Photoluminescence Tuning of Silica Nanoparticles Prepared by Electron Beam Irradiation and Their Applications. *Ceram. Int.* 2021, *47* (2), 2649–2655. https://doi.org/10.1016/J.CERAMINT.2020.09.113.

(6) Guleria, A.; Chiplunkar, S. S.; Hari, A.; Das, B.; Rath, M. C. Defect-Rich Silica Nanoparticles: Selective Enhancement of Blue Emission, Cr (VI) Sensing and Inherent Antioxidant Functionality. *Colloids Surf. A Physicochem. Eng. Asp.* 2025, *725*, 137599. https://doi.org/10.1016/J.COLSURFA.2025.137599.

(7) Menapace, I.; Mera, G.; Riedel, R.; Erdem, E.; Eichel, R. A.; Pauletti, A.; Appleby, G. A. Luminescence of Heat-Treated Silicon-Based Polymers: Promising Materials for LED Applications. *Journal of Materials Science 2008 43:17* 2008, *43* (17), 5790–5796. https://doi.org/10.1007/S10853-008-2882-9.

(8) Chang, H.; Park, Y.; Kim, K.; Han, C.; Yoon, Y.; Yoo, W.; Yoo, J.; Lee, D.; Han, H.; Kim, K.; Joo, J.; Kwon, W. Room-Temperature Phosphorescence of Defect-Engineered Silica Nanoparticles for High-Contrast Afterglow Bioimaging. *Chemical Engineering Journal* 2024, *493*, 152529. https://doi.org/10.1016/J.CEJ.2024.152529.

(9) Sun, Y.; Shao, X.; Sui, L.; Yang, Y.; Zhong, Y.; Yang, S.; Liu, J. Multi-Defects within Silica Inducing Coexistence of Thermal Activated Delayed Fluorescence and Room Temperature Phosphorescence. *Chemical Engineering Journal* 2025, *519*, 164772. https://doi.org/10.1016/J.CEJ.2025.164772.

(10) Trillot, S.; Tarrat, N.; Combe, N.; Benzo, P.; Bonafos, C.; Benoit, M. Evidence and Origin of Anomalous Diffusion of Ag+ Ion in Amorphous Silica: A Molecular Dynamics Study with Neural Network Interatomic Potentials. *Journal of Chemical Physics* 2025, *162* (10). https://doi.org/10.1063/5.0251120/3339199.

(11) Luo, Y.; Cui, C.; Zhang, X.; Jiang, Y.; Xiang, Z.; Ji, C.; Peng, Z. Carbon Dots-Based Fluorescence Assay for the Facile and Reliable Detection of Ag+ in Natural Water and Serum Samples. *Molecules* 2023, *28* (4), 1566. https://doi.org/10.3390/MOLECULES28041566/S1.

(12) Lu, S.; Li, Z.; Fu, X.; Xie, Z.; Zheng, M. Carbon Dots-Based Fluorescence and UV–Vis Absorption Dual-Modal Sensors for Ag+ and l-Cysteine Detection. *Dyes and Pigments* 2021, *187*, 109126. https://doi.org/10.1016/J.DYEPIG.2020.109126.

(13) Zhang, L.; Liao, D.; Fan, X.; Luo, B.; Jiang, L.; Qin, Y.; Liao, L.; Wang, Y.; Feng, L.; Li, Z.; Qin, A. Dual Photoluminescence Emission Chiral Carbon Quantum Dots for Ratiometric and Visual Fluorescent Ag+ Sensing. *ACS Appl. Nano Mater.* 2025, *8* (4), 1944–1955. https://doi.org/10.1021/ACSANM.4C06492.

(14) Wang, Y. Te; Wu, R. R.; Zhang, Y. Y.; Cheng, S. R.; Zhang, Y. High Quantum Yield Nitrogen Doped Carbon Dots for Ag+ Sensing and Bioimaging. *J. Mol. Struct.* 2023, *1283*, 135212. https://doi.org/10.1016/J.MOLSTRUC.2023.135212.

(15) Wu, Y. C.; Jiang, K.; Luo, S. H.; Cao, L.; Wu, H. Q.; Wang, Z. Y. Novel Dual-Functional Fluorescent Sensors Based on Bis(5,6-Dimethylbenzimidazole) Derivatives for Distinguishing of Ag+ and Fe3+ in Semi-Aqueous Medium. *Spectrochim. Acta A Mol. Biomol. Spectrosc.* 2019, *206*, 632–641. https://doi.org/10.1016/J.SAA.2018.05.069.